NASA/TM—2012-217621 AIAA–2011–1911

Macro Scale Independently Homogenized Subcells for Modeling Braided Composites

Brina J. Blinzler
University of Akron, Akron, Ohio

Robert K. Goldberg
Glenn Research Center, Cleveland, Ohio

Wieslaw K. Binienda
University of Akron, Akron, Ohio

July 2012

NASA STI Program . . . in Profile

Since its founding, NASA has been dedicated to the advancement of aeronautics and space science. The NASA Scientific and Technical Information (STI) program plays a key part in helping NASA maintain this important role.

The NASA STI Program operates under the auspices of the Agency Chief Information Officer. It collects, organizes, provides for archiving, and disseminates NASA's STI. The NASA STI program provides access to the NASA Aeronautics and Space Database and its public interface, the NASA Technical Reports Server, thus providing one of the largest collections of aeronautical and space science STI in the world. Results are published in both non-NASA channels and by NASA in the NASA STI Report Series, which includes the following report types:

- TECHNICAL PUBLICATION. Reports of completed research or a major significant phase of research that present the results of NASA programs and include extensive data or theoretical analysis. Includes compilations of significant scientific and technical data and information deemed to be of continuing reference value. NASA counterpart of peer-reviewed formal professional papers but has less stringent limitations on manuscript length and extent of graphic presentations.

- TECHNICAL MEMORANDUM. Scientific and technical findings that are preliminary or of specialized interest, e.g., quick release reports, working papers, and bibliographies that contain minimal annotation. Does not contain extensive analysis.

- CONTRACTOR REPORT. Scientific and technical findings by NASA-sponsored contractors and grantees.

- CONFERENCE PUBLICATION. Collected papers from scientific and technical conferences, symposia, seminars, or other meetings sponsored or cosponsored by NASA.

- SPECIAL PUBLICATION. Scientific, technical, or historical information from NASA programs, projects, and missions, often concerned with subjects having substantial public interest.

- TECHNICAL TRANSLATION. English-language translations of foreign scientific and technical material pertinent to NASA's mission.

Specialized services also include creating custom thesauri, building customized databases, organizing and publishing research results.

For more information about the NASA STI program, see the following:

- Access the NASA STI program home page at *http://www.sti.nasa.gov*

- E-mail your question to *help@sti.nasa.gov*

- Fax your question to the NASA STI Information Desk at 443–757–5803

- Phone the NASA STI Information Desk at 443–757–5802

- Write to:
  STI Information Desk
  NASA Center for AeroSpace Information
  7115 Standard Drive
  Hanover, MD 21076–1320

NASA/TM—2012-217621 AIAA–2011–1911

Macro Scale Independently Homogenized Subcells for Modeling Braided Composites

Brina J. Blinzler
University of Akron, Akron, Ohio

Robert K. Goldberg
Glenn Research Center, Cleveland, Ohio

Wieslaw K. Binienda
University of Akron, Akron, Ohio

Prepared for the
52nd Structures, Structural Dynamics, and Materials Conference
cosponsored by the AIAA, ASME, ASCE, AHS, and ASC
Denver, Colorado, April 4–7, 2011

National Aeronautics and
Space Administration

Glenn Research Center
Cleveland, Ohio 44135

July 2012

Acknowledgments

This work was funded by the Vehicle Systems Safety Technologies Program of the Aviation Safety Project, and NASA Graduate Student Researchers Program grant no. NNXD9AL95H.

Level of Review: This material has been technically reviewed by technical management.

Available from

NASA Center for Aerospace Information
7115 Standard Drive
Hanover, MD 21076–1320

National Technical Information Service
5301 Shawnee Road
Alexandria, VA 22312

Available electronically at http://www.sti.nasa.gov

Macro Scale Independently Homogenized Subcells for Modeling Braided Composites

Brina J. Blinzler
University of Akron
Akron, Ohio 44325

Robert K. Goldberg
National Aeronautics and Space Administration
Glenn Research Center
Cleveland, Ohio 44135

Wieslaw K. Binienda
University of Akron
Akron, Ohio 44325

Abstract

An analytical method has been developed to analyze the impact response of triaxially braided carbon fiber composites, including the penetration velocity and impact damage patterns. In the analytical model, the triaxial braid architecture is simulated by using four parallel shell elements, each of which is modeled as a laminated composite. Currently, each shell element is considered to be a smeared homogeneous material. The commercial transient dynamic finite element code LS-DYNA is used to conduct the simulations, and a continuum damage mechanics model internal to LS-DYNA is used as the material constitutive model. To determine the stiffness and strength properties required for the constitutive model, a top-down approach for determining the strength properties is merged with a bottom-up approach for determining the stiffness properties. The top-down portion uses global strengths obtained from macro-scale coupon level testing to characterize the material strengths for each subcell. The bottom-up portion uses micro-scale fiber and matrix stiffness properties to characterize the material stiffness for each subcell. Simulations of quasi-static coupon level tests for several representative composites are conducted along with impact simulations.

Nomenclature

σ_{11}	global axial (ultimate) tension stress
σ_{11A}	axial tension strength for subcells ‘A’ and ‘C’
$\sigma_{11A(pon)}$	axial tension strength for subcells ‘A’ and ‘C’ (point-of-nonlinearity)
$\sigma_{11(pon)}$	global axial (point-of-nonlinearity) tension stress
σ_{11B}	axial tension strength for subcells ‘B’ and ‘D’
σ_{22}	global transverse tension strength
σ_{22A}	transverse tension strength subcells ‘A’ and ‘C’
σ_{22B}	transverse tension strength subcells ‘B’ and ‘D’
ε_{11A}	axial tension failure strain subcells ‘A’ and ‘C’
ε_{11B}	axial tension failure strain subcells ‘B’ and ‘D’
ε_{22B}	transverse tension failure strain subcells ‘B’ and ‘D’
ε_{22A}	transverse tension failure strain subcells ‘A’ and ‘C’
S	compliance matrix
$[S]_{\mathrm{mod}}$	modified compliance
S_{11A}	compliance matrix (axial component) subcells ‘A’ and ‘C’
S_{11B}	compliance matrix (axial component) subcells ‘B’ and ‘D’
S_{12B}	compliance matrix (Poisson component) subcells ‘B’ and ‘D’
S_{12A}	compliance matrix (Poisson component) subcells ‘A’ and ‘C’
S_{22B}	compliance matrix (transverse component) subcells ‘B’ and ‘D’
S_{22A}	compliance matrix (transverse component) subcells ‘A’ and ‘C’
E_{22A}	transverse elastic modulus subcells ‘A’ and ‘C’
E_{11}	longitudinal elastic modulus
E_{22}	transverse elastic modulus
ν_{12}	in-plane Poisson’s ration
G_{12}	in-plane shear modulus
G	shear modulus
E	elastic modulus
β	decay constant
υ	Poisson’s ratio
$\dot{\varepsilon}$	strain rate
σ_{ult}	ultimate stress

Introduction

Polymer matrix composite materials are utilized for a variety of aerospace applications because of their comparatively lower weight, and versatile material properties. Composite structures may undergo a variety of loading conditions during service life. In order to be used as protective structures, composites are required to resist ballistic impact loading. For these types of applications, it is necessary to have a model that accurately simulates both ballistic limit and damage patterns for the impact region. The ballistic limit of a structure is the point at which a projectile travels completely through the material but the projectile's residual velocity nominally equals zero. The ballistic limit is generally a range determined from a full array of impact experiments. Every composite material behaves differently under impact loading conditions. The ballistic limit and damage mechanisms are highly dependent on the material constituents, the structure's layup, the textile architecture, and the shape of the projectile. Specifically, in a braided composite, numerous micromechanical phenomena occur contributing to both the ballistic limit and the damage patterns.

There has been a significant amount of research conducted in the analysis and modeling of textile composites. The majority of the efforts have concentrated on various means to determine the effective mechanical properties of woven materials. Among the earliest attempts to model these material was the work of Chou and Isikawa (Ref. 1). In their original mosaic model, the woven composite was approximated as a one-dimensional series of laminated cross-ply composites, and classical lamination theory in combination with iso-stress or iso-strain assumptions was applied to obtain the effective stiffness properties of the material. They later extended the model to account for the fiber undulations that are present in an actual woven material (Ref. 1). This approach was extended to two dimensions by Naik and Shembekar (Ref. 2), where a mixture of parallel and series assumptions were applied to obtain the effective properties of the material. To analyze more complicated fiber architectures, such as braided composites, researchers such as Pastore and Gowayed (Ref. 3) and Byun (Ref. 4) modeled the fibers as a series of rods at various angles, and utilized simple iso-strain assumptions to obtain the overall effective properties of the composite. Using a different approach, Rao et al. (Ref. 5) developed a method where each subcell possesses a modified geometry of the portion of the textile geometry. Also, Walter et al. (Ref. 6) discusses an experimental study which details how the global response of textile composites can be correlated to the local damage mechanism in the matrix and fiber tows. More sophisticated analysis methods, such as those developed by Tanov and Tabiei (Ref. 7), Bednarcyk and Arnold (Ref. 8), Sankar and Marrey (Ref. 9), and Jenq and Mo (Ref. 10) used an approach where a representative unit cell of a woven composite was created, and then micromechanics-based approaches were applied to compute the effective properties and response of the material. In the context of applying these methods within a finite element model, elements are created with a homogenized set of material properties, and the appropriate analysis method is used to generate the effective properties and response of the woven material.

Traditionally, when these analytical methods are used in combination with finite element analysis of a structure composed of woven or braided composite materials, homogenized elements are used, in which the architecture of the textile material is not directly accounted for within the finite element model. The braided composites analyzed in this paper have a large unit cell size, as can be seen in Figure 1 (unit cell: 17.8- by 5.1-mm). Because of this large unit cell size, the materials experience strain and damage more like structures rather than homogenized materials. For this reason the high velocity impact damage patterns are highly dependent on the material architecture and projectile shape. Classical analysis methods cannot account for these architecture and shape effects. In an attempt to develop a capability to simulate the architecturally-dependent damage patterns observed in triaxially-braided composites under impact conditions, Cheng created a "Braided through the Thickness Approach" (Ref. 11), where a braided composite was modeled as a series of layered shell elements, and each element was a laminated composite with the appropriate layup. The approach was developed to analyze triaxially-braided composites with a [+60°/0°/–60°] braid architecture. A limitation of Cheng's method was that it had to be calibrated with full impact testing for each material analyzed. Cheng's method needed to be improved to systematically calculate the material properties required by the finite element material model based on coupon level experimental results. The focus of this paper is to fill this need for quasi-isotropic triaxial braided carbon-epoxy composites. However, the methodology which will be presented is applicable to other triaxially braided fiber architectures or theoretically any textile composite architecture.

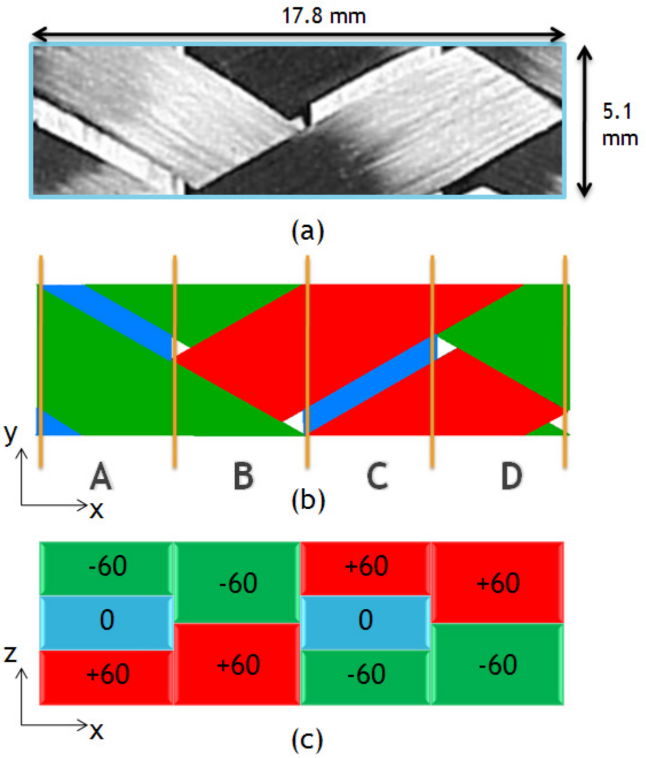

Figure 1.—Identification of the unit cell (a)specimen photograph, (b) four shell elements (A,B,C,D), (c) through thickness layers

One application for triaxially-braided composite materials is for use in jet engine fan blade containment systems. To create an optimum engine case design, the failure, damage, and deformation needs to be simulated with the use of commercial explicit finite element codes. A design tool is required to capture the structural effect of the braid and damage along fiber bundles while modeling the entire engine case. In order to balance these needs, a macro scale finite element simulation technique was developed employing an advanced continuum damage mechanics material model in the finite element code LS-DYNA (Ref. 12). For these aerospace applications, the model needed to accurately simulate the textile composite under both static loading and impact loading situations. The unique way the fiber architecture was incorporated into the finite element analysis will be discussed later. A triaxially-braided composite with a [+60°/0°/–60°] layup was investigated. The braided composites under consideration for this study have six plies through the thickness. In the braided composites, the 0° fibers have 24k filaments per tow, while the +60° and –60° fibers have 12k filaments per tow. A unit cell for a typical triaxially-braided fiber preform is shown in Figure 1(a). In Figure 1, the ±60° bias fibers are visible on the surface. Portions of the 0° axial fibers that lie below the bias fibers can be seen in the open spaces between the bias fibers. An assumption in the methodology is that the fiber bundle spacing and number of fibers per fiber bundle are adjusted such that the fiber volume fractions in both the axial and bias directions are equal. In actuality, this particular fiber architecture is quasi-isotropic in-plane. Therefore, the global in-plane stiffness should be the same in all directions, but this condition is not actually enforced within the context of the analysis model.

Approach

Previous research in modeling architecturally-dependent damage in braided composites was conducted by Cheng (Ref. 11) and Littell (Ref. 13). Their analytical models discretized the braided composite into a series of parallel shell elements. Each of these elements were modeled as laminated composites (Ref. 14). The use of layered shell elements allowed for architecturally-dependent damage to be modeled while maintaining computational efficiency. However, Littell (Ref. 13) approached the analysis with a different method. He used a top-down method to back out stiffness and strength properties from experimental coupon level data. In addition, Littell attempted to approximate the ply shifting that has been observed in braided composites by his discretization method. There were some difficulties implementing the discretization method, and the irregular damage patterns of the braided composites could not be captured. In the current study, to improve the simulation tool, a top-down approach for determining the strength properties was merged with a bottom-up approach for determining the stiffness properties. In order to resolve discretization issues, independently homogenized shell elements were used, where each element is modeled as a smeared continuum with a set of homogenized stiffness and strength properties. Each subcell in the model is defined to have different homogenized properties, which allows for the simulation of architecturally-dependent damage. In the top-down approach, all of the information needed to characterize the material strengths was taken from the global strengths obtained from macro-scale experimental quasi-static coupon tests. In the bottom-up approach, the information needed to characterize the material stiffness was taken from micro-scale fiber and matrix stiffness properties.

To apply the analysis approach, the braided fiber architecture is idealized. As a first step in this process, a schematic of the top view of the fiber architecture is shown in Figure 1(b). As shown in Figure 1, the unit cell is divided into four parallel subcells. Next, each subcell is approximated to be a laminated composite composed of a stack of fiber tows at various orientations that are determined by the braid architecture (Figure 1(c)). Subcell A is modeled as a [+60°/0°/–60°] composite (bottom layer listed first). Subcell B is modeled as a [+60°/–60°] composite, subcell C is modeled as a [–60°/0°/+60°] composite, and subcell D is modeled as a [–60°/+60°] composite. For subcells A and C, the fact that the 0° fiber tows have twice as many filaments per tow as the +60° and –60° layers is accounted for by making the 0° layer twice as thick as the remaining two layers. Li, et al. (Ref. 15) have examined using more subcells with this type of analysis approach to more accurately simulate the fiber undulations which are present in the actual composite. However, increasing the number of subcells used to model the unit cell increases the computational cost of applying the methodology, especially when applied to realistic structural configurations. Furthermore, each subcell could be broken up into several elements, and preliminary investigation into mesh refinement has yielded equivalent results. Also, results to date have indicated that further discretization is not required to obtain acceptable results. Any pure matrix pockets present in the composite are not modeled explicitly, but are instead incorporated into the effective properties of each layer within the subcell, affecting the effective fiber volume ratio of each subcell. Xiao, et al. (Ref. 16) developed a similar model in which the pure resin pockets are explicitly modeled as layers of pure matrix. In the future, such an approach may be attempted for this method to determine whether the simulation results can be improved.

Each subcell is modeled as an individual shell element in a finite element model. The unit cell thus consists of four shell elements. The assumption of using shell elements is justified since the length and width of typical structures composed of these materials are much greater than the thickness. Impact tests conducted by Littell (Ref. 13) noted that the out-of-plane deformation in flat panel impact tests was found to be relatively small in relation to the panel dimensions. In addition, the availability of appropriate constitutive models for composites using solid elements in transient finite element codes such as the commercial software LS-DYNA (Ref. 12) are limited. Future efforts may involve developing an appropriate constitutive model suitable for use with solid elements. A full structure can be modeled by replicating this four element unit cell throughout the finite element mesh.

Material Model

The finite element software used in the analysis is LS-DYNA (Ref. 12). LS-DYNA is a commercially-available transient dynamic finite element solver, which contains contact algorithms for ballistic impact modeling (Ref. 12). This solver also contains a number of material models for simulating composites. One of these is a laminated composite material model for composite shell elements derived from Matzenmiller's (Ref. 17) method. Matzenmiller (Ref. 17) developed a plane-stress constitutive model for anisotropic damage of fibrous composite materials with nonductile matrices. The method employed continuum damage mechanics theory in the material axis system to approximate damage initiation and ultimate material failure. Each element was assumed to be a laminated composite, and any nonlinearity was assumed to be due to damage mechanisms. The development of damage was completely dependent on the stress and strain states of the individual unidirectional lamina. Matzenmiller then adopted the Hashin failure criteria, which determined a failure envelope based on the five strength properties of the unidirectional lamina: longitudinal tension, longitudinal compression, transverse tension, transverse compression, and shear strength (Ref. 18). The equations used in the LS-DYNA material model *Mat_58 reflect the Matzenmiller method and assumptions (Ref. 12).

The required inputs for the *Mat_58 material model are based on material axis system properties. The properties required by this model are properties of the homogenized laminate (the equivalent properties of each element). A fundamental problem in the analysis of textile composites is that the lamina properties are not known and cannot be directly measured. To characterize the composite material the "Independently Homogenized Subcells" method was developed. This method back-calculates lamina properties from experimental results and computes a set of homogenized properties for each of the subcells listed in Figure 2: subcells 'A', 'B', 'C', and 'D'. The equivalent properties seen in Table 1 were calculated employing the "Independently Homogenized Subcells" method. It should be noted that the "In Plane Poisson Ratio" required for the material model and listed in the table is ν_{21} not ν_{12}. There are stress limiting parameters, which allow for the material to accumulate strain even after the maximum stress is reached in addition to these inputs in the *Mat_58 material model. These particular parameters will be discussed in greater detail later. There are several advantages for using this approach. The constitutive model that was utilized is a continuum damage mechanics model, an important quality for impact analysis. The experimental data required for characterizing strength comes solely from tests on the triaxially braided composite samples; no additional inputs are required. In addition, the model is computationally efficient, and can be employed to model large components.

The stiffness and strength inputs for the material model are listed in Table 1. For the current system the material inputs required by the *Mat_58 model are material axis system strength and stiffness properties. Many of the properties needed for inputs in the material model are not directly measurable. An equivalent unidirectional laminate cannot be made and tested that represents the braided composite. The method of combining a top-down approach with a bottom-up approach to determine the required properties was formed to fill this need.

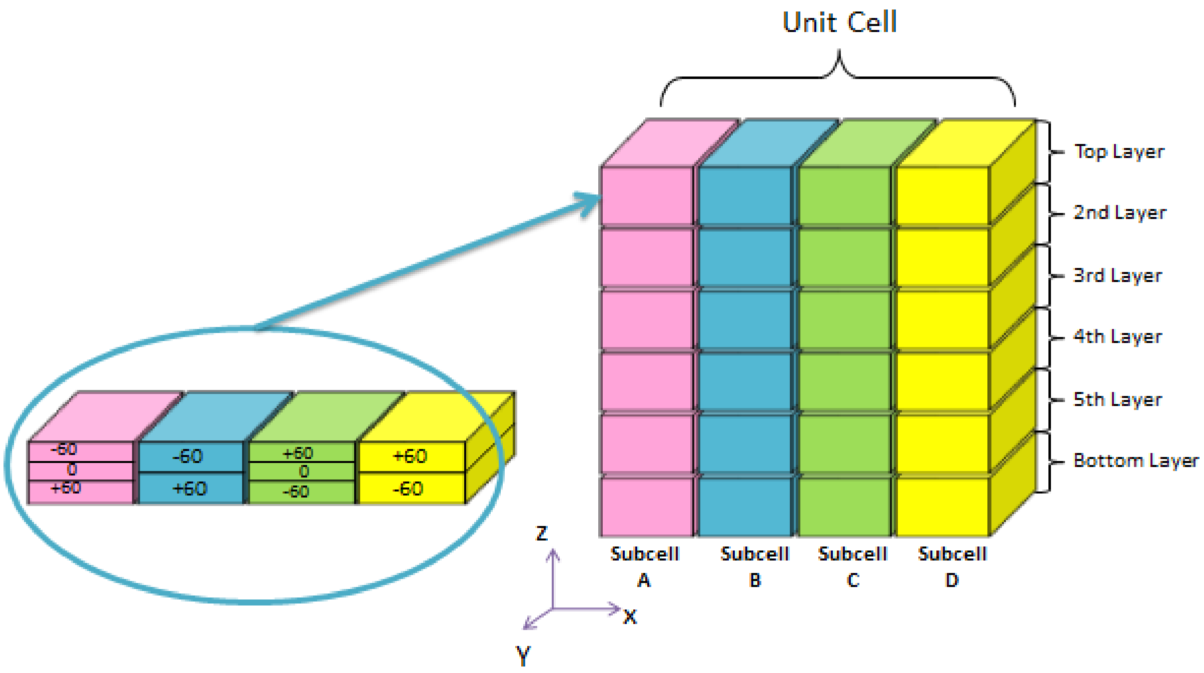

Figure 2.—Schematic of subcell discretization of six layer triaxial braided composite.

TABLE 1.—CALCULATED MATERIAL PROPERTY VALUES
USED FOR THE QUASI-STATIC COUPON SIMULATIONS

Material	T700 – PR520		T700 – E862		T700 – 5208		T700 – 3502	
Material parameter name	(MPa)		(MPa)		(MPa)		(MPa)	
Subcell	A&C	B&D	A&C	B&D	A&C	B&D	A&C	B&D
Axial modulus (E_{11})	96580	8567	95367	6398	96403	8253	96224	7934
Transverse modulus (E_{22})	39577	38032	38276	31830	39393	37194	39204	36322
In plane shear modulus (G_{12})	17388	23618	16525	23066	17264	23537	17136	23455
In plane Poisson ratio (ν_{21})	0.127	1.427	0.127	1.634	0.127	1.454	0.127	1.482
Axial tensile failure strain (ε_{11T})	0.020	0.020	0.016	0.016	0.013	0.013	0.012	0.012
Axial compressive failure strain (ε_{11C})	0.019	0.019	0.012	0.012	0.005	0.005	0.010	0.010
Transverse tensile failure strain (ε_{22T})	0.054	0.017	0.043	0.013	0.036	0.011	0.033	0.010
Transverse compressive failure strain (ε_{22C})	0.015	0.009	0.010	0.006	0.007	0.005	0.009	0.005
In plane shear failure strain (ε_{12})	0.028	0.020	0.023	0.017	0.023	0.017	0.016	0.012
Axial tensile stress at failure (σ_{11T})	1925	171	1537	62	1290	103	1189	80
Axial compressive stress at failure (σ_{11C})	694	62	632	42	459	39	670	55
Transverse tensile stress at failure (σ_{22T})	1048	1048	800	800	696	696	634	634
Transverse compressive stress at failure (σ_{22C})	346	346	305	305	215	215	242	242
In plane shear stress at failure (σ_{12})	308	308	257	257	308	308	224	224

Determination of Material Properties

To accurately assign properties to the individual elements (subcells) in the finite element simulation, an analytical algorithm called “Independently Homogenized Subcells” was developed. This algorithm was developed to calculate material axis system inputs for *MAT_58 from the fiber and matrix stiffness properties, and the global quasi-isotropic coupon test strengths. The use of this type of algorithm to compute inputs for the finite element simulation facilitates the simulation of architecturally-dependent damage by defining the various subcells of the model as having different mechanical properties. Subcells ‘A’ and ‘C’ have similar configurations only vertically inverted (Figure 2). Subcells ‘B’ and ‘D’ also have similar configurations only, again, vertically inverted. Therefore, only two sets of properties must be calculated. One set of mechanical properties is calculated for subcells ‘A’ and ‘C’, while another set is calculated for subcells ‘B’ and ‘D’. These mechanical properties, calculated though rigorous micromechanical and composite laminate theories were adapted to characterize the material properties used in the braid architecture approach developed by Cheng (Ref. 11) and Littell (Ref. 14).

The next six sections contain a detailed account of the inner workings of the “Independently Homogenized Subcells” program. In Figure 3, the pseudocode is presented, and each subroutine is labeled. The following paragraphs explain the algorithms of the individual subroutines employed.

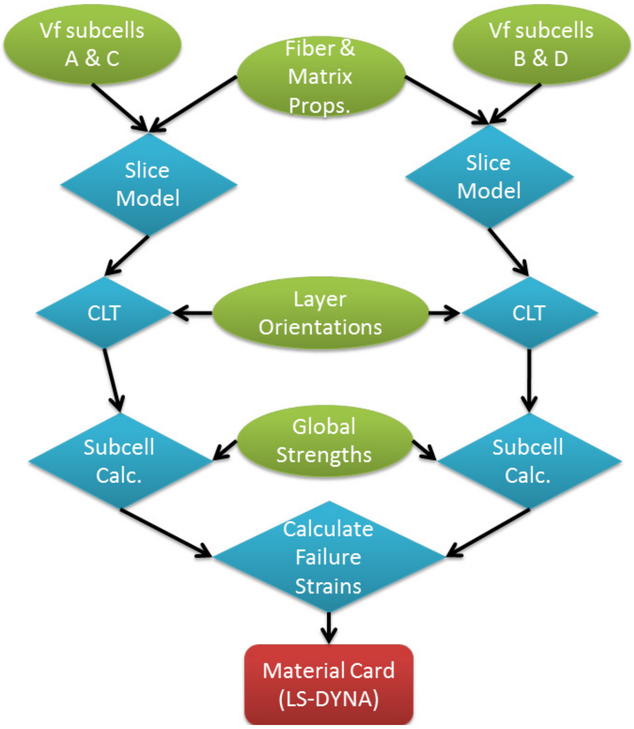

Figure 3.—Independently homogenized subcells pseudocode.

Inputs

The inputs needed for the “Independently Homogenized Subcells” program are indicated in Figure 3 by green ovals. These inputs were the fiber volume ratios of the subcells, fiber and resin stiffness properties, lamina orientations, and global strengths of the composite. For this study, the average fiber volume ratio for each subcell and the fiber volume ratio for individual plies within each subcell, were determined based on high-fidelity finite element models of triaxially-braided composites developed by Li, et al. (Ref. 15). In this model, various dimensions for the unit cell and the fiber tows were taken from optical micrographs, and a finite element model with average dimensions was constructed. To compute the required finite element ratios for the "Independently Homogenized Subcell" program, the finite element mesh of Li, et al. (Ref. 15) was virtually divided into subcells and layers within the subcell (including the fiber tow and resin rich regions). The percentage of elements of a given material type (fiber tow or matrix) within each subcell and subcell layer was then computed. Given an assumed fiber volume fraction within the fiber tow, and knowing an overall fiber volume ratio for the composite, average fiber volume ratios for each subcell and the individual layers within each subcell (assuming that the subcell layer consists of the fiber tow and pure resin regions) were computed. Other approaches have been developed by Liu, et al. (Ref. 19) and Xiao, et al. (Ref. 16) in which the unit cell geometry and dimensions as measured by micrographs are explicitly used to determine the required subcell and layer fiber volume ratios within the unit cell. These approaches will be applied in the future to the current method to see if improved geometry and fiber volume ratio values can be obtained. Through Li's virtual experiments, volume fractions of the axial plies in subcells 'A' and 'C' were identified as 0.80, and the volume fractions of the bias plies in all subcells were identified as 0.50 (Ref. 15). The fiber and matrix constituent stiffness properties were given by the composite manufacturer (Ref. 13) (Table 2). The lamina orientations are listed in Figure 2. The global strengths were obtained from the quasi-static coupon test properties (Table 3) (Ref. 13).

Stiffness Properties

The first step was to utilize Goldberg's Slice Model (Ref. 20) to create effective unidirectional lamina stiffness matrices for the composite laminates employed to represent each subcell. This model is a micromechanics model developed for use in calculating effective composite properties (Ref. 20). This method was employed due to its simplicity and accuracy. The Slice Model calculates effective unidirectional ply properties from the fiber volume fraction, and the fiber and matrix stiffness properties. This model was employed to determine the stiffness of a single ply within a subcell. The calculation for the stiffness of a single ply was performed for the 'A' and 'C' subcells, and the 'B' and 'D' subcells independently.

Classical lamination theory (CLT) (Ref. 21) was then employed to compute the overall effective laminate stiffness matrices for each subcell. The effective stiffness matrices of the unidirectional laminae calculated in the previous process were utilized for the calculations. Only in-plane loads were assumed to be applied. Therefore, the moment curvature relations of classical laminate theory were neglected. In-plane normal-shear couplings were neglected as well, because the subcells were approximated as balanced laminates. In addition, tension-bending coupling was neglected even though the composite layups were anti-symmetric, because no out-of-plane bending was observed in testing when in-plane strains were applied. Further, in the global braided material, the composite was approximately symmetric, which resulted in the elimination of the tension-bending coupling. From the calculated laminate stiffness matrices, the overall stiffness matrix, moduli, and Poisson's ratio for each subcell were then computed assuming orthotropic material behavior. As previously noted, in the actual triaxially-braided composite, the zero degree fiber bundles contained twice as many fibers as the bias fiber bundles. To account for this, in subcells 'A' and 'C', the zero degree laminae were given twice the thickness of the bias laminae in the composite stiffness matrix calculations. These effective stiffness properties were then applied as the stiffness inputs for the finite element model.

TABLE 2.—CONSTITUENT PROPERTIES

	E_{11}, GPa	E_{22}, GPa	ν_{12}	G_{12}, GPa
T700 (fiber)	230.00	15.00	0.20	27.00
PR520 (resin)	4.00	4.00	0.36	1.47
E-862 (resin)	2.70	2.70	0.36	1.47
5208 (resin)	3.80	3.80	0.36	1.47
3502 (resin)	3.60	3.60	0.36	1.47

TABLE 3.—GLOBAL STRESS VALUES USED IN CALCULATIONS

(MPa)	T700/PR520	T700/E862	T700/5208	T700/3502
Global stress at failure (axial tension)	1048	800	696	634
Global stress at failure (transverse tension)	1048	800	696	634
Global stress at failure (axial compression)	378	337	249	363
Global stress at failure (transverse compression)	346	305	215	217
Global stress at failure (shear)	308	257	308	224
Stress at pt. of nonlinearity (axial tension)	1048	495	650	524
Global strain-at-failure (axial compression)	0.019	0.012	0.005	0.010
Global strain-at-failure (transverse compression)	0.012	0.008	0.006	0.007
Global strain-at-failure (shear)	0.024	0.020	0.020	0.014

Strength Properties—Axial Tension

The third subroutine in the "Independently Homogenized Subcells" program identified the global strengths needed to back-calculate the subcell strengths and then computed those properties. These properties can be seen in Table 3. The global strength properties were utilized to run the "Subcell Calculations." The global stresses, the effective laminate stiffness properties from the previous step, and various uniform stress-strain assumptions between subcells were employed to calculate homogenized strengths for each subcell. Because these subcells have equivalent properties the same material was characterized for both 'A' and 'C'. This was also the case for subcells 'B' and 'D'. Therefore, there were only two independent materials to characterize. Separate subroutines of the "Subcell Calculations" were run for axial, transverse, and shear loading cases.

To calculate the axial tension strength in the subcells, both the stress at failure and the stress at the point where the stress-strain curve becomes nonlinear were used. For three out of the four materials, at a particular stress level, significant stiffness degradation occurred, reflected in the stress-strain curves becoming nonlinear. For example, as shown in Figure 4, for the T700/3502 material, this stiffness degradation (point-of-nonlinearity) occurs at a stress level of 524 MPa. The point where the stress-strain curve becomes nonlinear was identified by Littell (Ref. 13) as being correlated to the stress level where there is a significant amount of bias fiber bundle splitting (local matrix microcracking) and out of plane deformation. This phenomenon was simulated in the analysis model by assuming that failure in subcells 'B' and 'D' occurred at the global stress level where the stress-strain curve became nonlinear given that these subcells contain bias fibers only. Therefore, the stress at the point of nonlinearity was used to compute the strength for subcells 'B' and 'D'. For subcells 'A' and 'C', the axial strength in the subcells was calculated employing the ultimate axial tension failure stress.

To account for the fact that the overall composite does not fail even after subcells 'B' and 'D' reach their maximum stress, the "stress limiting parameter" available in the *MAT_58 material model was used. By setting this parameter to "1" for the case of axial tension in subcells "B" and "D", the subcells could continue to accumulate strain even after the maximum stress in the subcells was reached. Catastrophic failure occurs experimentally in the axial tension test specimen only when the axial fibers break (Ref. 13), which is represented in the current model as resulting in failure in subcells 'A' and 'C'. A visualization of how the SLIMT1 parameter changes the simulation results is shown in Figure 5. It can be seen in the figure that the subcells 'B' and 'D' continue to elongate until the subcells 'A' and 'C' fail, resulting in all of the subcells failing at the same axial tensile strain.

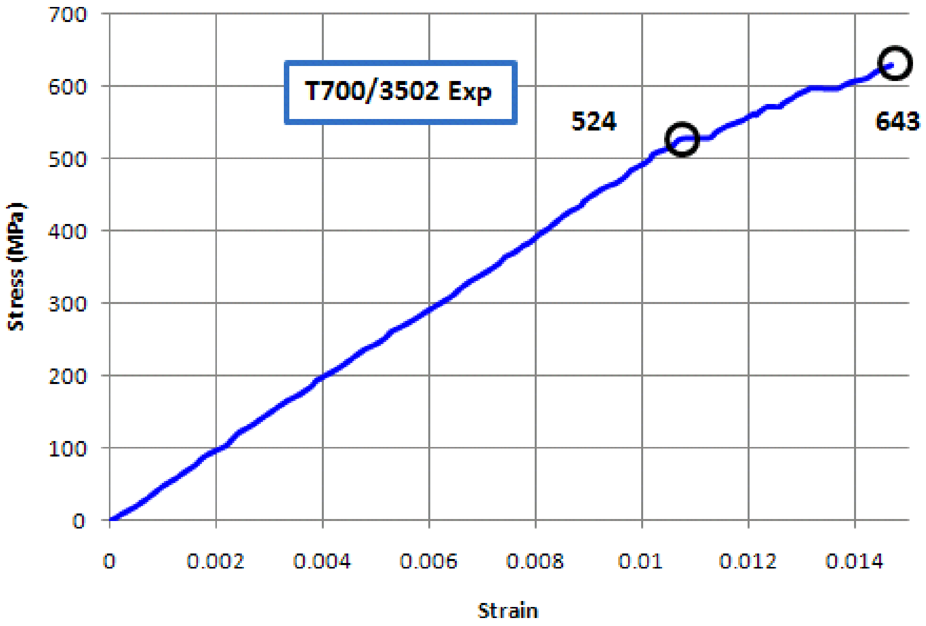

Figure 4.—Axial tension experimental coupon test for the T700/3502 material which demonstrates stiffness degradation.

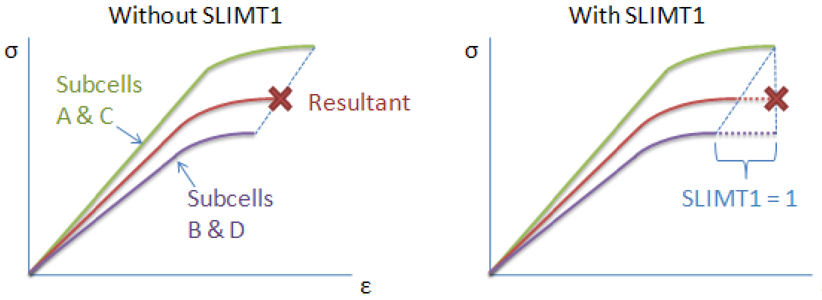

Figure 5.—Illustration of the SLIMT1 (Stress Limiting Parameter in Axial Tension).

The global strength from the axial tension coupon test where significant stiffness degradation occurs (point-of-nonlinearity), was used to calculate the axial tension strength in subcells 'B' and 'D'. Using mechanics of materials theory and appropriate uniform stress and uniform strain assumptions, the following equations were derived to compute the partitioned subcell stress. The axial tension stress in subcells 'A' and 'C' at the point-of-nonlinearity (PON) was calculated using Equation (1). The axial tension strength in subcells 'B' and 'D' was then calculated using Equation (2)

$$\sigma_{11A(pon)} = \sigma_{11(pon)} /(0.5\ (1 + S_{11A}/S_{11B})) \qquad (1)$$

$$\sigma_{11B} = S_{11A}/S_{11B}\ \sigma_{11A(pon)} \qquad (2)$$

The axial tension failure strength of subcells 'A' and 'C' were computed using the axial tension failure stress for the overall composite and the failure strength of subcells 'B' and 'D' by using Equation (3)

$$\sigma_{11A} = 2\ (\sigma_{11} - 0.5\ \sigma_{11B}) \qquad (3)$$

This equation is based on the assumption that the failure of subcells 'A' and 'C' results in the ultimate axial tensile failure of the composite and that at this point the stress in subcells 'B' and 'D' remain at their computed maximum value. The axial tension failure strain for both subcells 'A' and 'C' and subcells 'B' and 'D' were assumed to be equal to the global axial tension failure strain obtained from the experiments, as shown in Equations (4) and (5).

$$\varepsilon_{11A} = \varepsilon_{11} \qquad (4)$$

$$\varepsilon_{11B} = \varepsilon_{11A} \qquad (5)$$

To calculate the axial compression strength in the subcells, expressions similar to Equation (1) and (2) were used. The global composite axial compressive failure stress was used in the computations due to the assumption that all of the subcells failed at the global composite axial compressive failure strain. The axial compressive failure strains were set equal to the global axial compression failure strains obtained from experiments.

Strength Properties—Transverse Tension

As discussed by Littell (Ref. 13), triaxially-braided composite transverse tensile tests conducted on straight-sided coupons may not yield results that are truly representative of the actual material response. Specifically, the transverse tension tests yielded ultimate strengths much lower than the expected values. More discussion about the transverse tension coupon tests can be found in Reference 13. For this reason, the experimental test results in transverse tension were not used in this method. The calculations were instead based on the ultimate stress obtained from the axial tension coupon test. The transverse tension failure stress was assumed to be equal to the axial tension failure stress due to the theoretical quasi-isotropy of the materials. Using mechanics of materials theory the following equations were derived to calculate the partitioned subcell stresses. The transverse tension strengths for the individual subcells were then set equal to the global assumed transverse tension strength, as shown in Equations (6) and (7).

$$\sigma_{22A} = \sigma_{22} \qquad (6)$$

$$\sigma_{22B} = \sigma_{22} \qquad (7)$$

The transverse tension failure strain for subcells 'B' and 'D' was calculated using Equation (8). Because of the orientation of the zero-degree ply fiber bundles, these bundles experience large transverse elongation during transverse tension testing due to axial fiber splitting and local matrix micro cracking (Ref. 13). Based on these mechanisms, it is postulated that the zero-degree ply bundles carry almost no load at the point where the overall composite fails in transverse tension. To incorporate this effect into the finite element simulation, the compliance matrix of the zero-degree ply bundles was adjusted by setting the transverse elastic modulus of the zero degree layers in subcells 'A' and 'C' to fifty percent of the nominal value as shown in Equation (9). Using this value, a modified compliance matrix was assembled as shown in Equation (10) (Ref. 21). The transverse tension failure strain for subcells 'A' and 'C' was then calculated using this modified compliance matrix. This failure strain for subcells 'A' and 'C' was calculated using Equation (11).

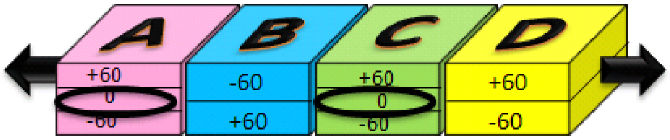

Figure 6.—Image of the unit cell in transverse tension.

$$\varepsilon_{22B} = S_{12B}\,(S_{12A} - S_{12B})/(S_{11A} + S_{11B})\,\sigma_{22} + S_{22B}\,\sigma_{22} \qquad (8)$$

$$S_{22A} = 2\,(1/E_{22A}) \qquad (9)$$

$$[S]_{\text{mod}} = \begin{bmatrix} 1/E_{11} & -\nu_{12}/E_{11} & 0 \\ -\nu_{12}/E_{11} & 2/E_{22} & 0 \\ 0 & 0 & 1/G_{12} \end{bmatrix} \qquad (10)$$

$$\varepsilon_{22A} = S_{12A}\,(S_{12B} - S_{12A})/(S_{11A} + S_{11B})\,\sigma_{22} + S_{22A}\,\sigma_{22} \qquad (11)$$

Strength Properties—Compression and Shear

Transverse compression and shear strengths for the subcells were assigned to the subcells in the same way as for the transverse tension strength, with the subcell strengths being set equal to the global composite failure stress. The subcell failure strains were calculated as follows. For the cases of transverse compression, axial compression, and in-plane shear, examinations of the optical strain data obtained during tests conducted by Littell (Ref. 13) indicated that the strain field was uniform throughout the gage section. Therefore, all four of the subcells were assumed to fail simultaneously. Because of the highly nonlinear characteristics of the experimental transverse compression, axial compression, and in-plane shear curves, the subcell failure strains of these curves were computed based on the experimental global composite failure strain data, specifically the values indicated in Table 3. The transverse compression and shear failure strains for each subcell were computed by multiplying the global composite failure strains by a scale factor determined by applying uniform strain and stress assumptions and mechanics of materials theory. In these calculations the actual ratios of the failure strains in the subcells are assumed to be equivalent to the ratios of the failure strains in each subcell computed using the failure stresses and elasticity theory.

The “Independently Homogenized Subcells” method is a rigorous and repeatable approach. This method was developed based on accepted theoretical algorithms and methods, and can easily be adapted to calculate material inputs for any woven or braided composite.

Quasi-Static Coupon Simulations

A series of simulations was conducted to evaluate the analysis methods described above and to check the correlation of the computed stiffness and strength input parameters. Specifically, quasi-static axial and transverse coupon level tensile tests and quasi-static axial and transverse compression tests on four representative triaxially-braided composites were simulated. The materials were composed of a two-dimensional triaxially-braided preform and a 177 °C cure epoxy resin. For both materials, TORAYCA T700S fibers (Toray Carbon Fibers America, Inc.), a high strength standard modulus carbon fiber was used. For the first material, EPICOTE Resin 862/EPIKURE Curing Agent W system (Hexion Specialty Chemicals) (E-862 for short), a two-part low viscosity system was used. For the second material, CYCCOM PR 520 (Cytec Industries, Inc.), a one-part toughened resin was used. Cytec’s 5208 resin and Hexcel’s 3520 resin were used for the remaining two material systems.

For the composites under consideration, six layers of a [+60°/0°/–60°] braided preform were stacked on top of one another. The axial fibers were 24k flattened tows while the bias fibers were 12k flattened tows. Again, the differing sizes of the fiber bundles were accounted for within the subcell discretization by making the layers with axial fibers twice as thick as the layers with bias fibers in subcells A and C. The global fiber volume fraction for all of the triaxially-braided composites was determined to be approximately 56 percent.

The experimental tests were conducted by Littell, et al. (Ref. 14), where full details of the experimental procedures can be found. Displacement-controlled tests were conducted. A minimum of five tests were conducted in each direction for each material system. In the figures to follow, the test results plotted are representative of specific tests which yielded results near the average. As mentioned earlier, future efforts will involve determining a more statistically based “mean results curve” for the various tests that were conducted.

For the analytical simulations, to compute the stiffness properties for each subcell, first the fiber volume ratio in each layer of each subcell was computed using the methods described above. By using the specified procedures, the fiber volume ratio of the axial layers in subcells A and C were determined to be 0.80, and the fiber volume ratio of the layers with bias fibers in all of the subcells was determined to be 0.50. The specified micromechanics methods and classical laminate theory were then applied to compute the effective stiffness properties for each subcell. In applying the micromechanics analysis methods, the stiffness properties for the fiber and matrix given in Table 2 (and taken from Littell (Ref. 13)) were applied. The applied constituent properties were obtained from a combination of manufacturer’s data and representative values for carbon fibers obtained through various micromechanics analysis methods. The computed stiffness properties for each subcell for all of the material systems studied are listed in Table 1. Note that the Poisson’s ratio listed is the transverse Poisson's ratio, ν_{21}, which is required for the LS-DYNA material model, which explains the large Poisson's ratio values shown in the table. Also, note that the given properties are the smeared homogeneous properties for each subcell. One consequence of this approximation is that the transverse modulus is much higher than the longitudinal modulus for subcells B and D due to the bias fiber-dominated layup of these subcells. As already mentioned, these values are average values taken from representative tests conducted by Littell (Ref. 13) for each material. Future efforts will involve conducting a detailed statistical study of the global composite coupon results in order to obtain statistically-significant mean and extreme values to use in the analysis.

The axial and transverse tension simulations, seen in Figure 7, were developed to mimic experimental coupon tests. For these static simulations, the nodes at the very top were fixed. Displacement in the static simulations was applied to the nodes at the bottom in the direction of the loading arrows. The dimensions of both axial tension and transverse tension simulations are 30.48-cm (12.00-in.) by 3.58-cm (1.40-in). The axial tension simulation is composed of 480 elements, 8 across and 60 long. The transverse tension simulation is composed of 476 elements, seven across and 68 long. The stress-strain curves for these simulations were defined by averaging the elemental stresses and strains for the bottom six rows of elements in each model.

To calibrate the material properties for the composites examined in this study, simulations of the axial tension and transverse tension coupon tests were carried out and results from the axial tension simulations were compared with experimental data from quasi-static coupon tests conducted by Littell (Ref. 13). The material properties used in the analyses are shown in Table 1.

Figure 8 to Figure 15 display the results of the simulations for each of the materials examined in this study, and comparisons of the coupon simulation results (red) with the experimental coupon stress-strain curves (blue) are shown for the axial tension analyses. Figure 8, Figure 10, Figure 12, and Figure 14 contain the axial tension curves for the composite materials T700/PR520, T700/E862, T700/5208, and T700/3502, respectively. The computed axial tension values for the T700/PR520 composite compare well with the experimental axial tension test curve as shown in Figure 8. Overall the simulation is slightly stiffer and fails at a slightly lower stress than the experiment shows, however, the area under the curve is similar. Therefore, the amount of energy absorption compares very well the experiment and this is an important aspect for impact simulation. The computed axial tension values for the T700/E862 composite also compares well with the experimental axial tension test curve as shown in Figure 10. Again for the T700/E862 composite the simulation is slightly stiffer and weaker than the experimental results, but the area under the curve is equivalent. The nonlinearity of the stress-strain curve is also captured by the simulation. The computed axial tension composite coupon response for the T700/5208 material also compares well with the experimental axial tension test curve as shown in Figure 12. The simulation does not capture the stiffening observed in the experiment, but that may be an artifact of the experimental results. The computed axial tension coupon response for the T700/3502 composite also compares well with the experimental axial tension test curve as shown in Figure 14. Again for the T700/3502 material the simulation is slightly stiffer and weaker, the area under the curve is nearly equivalent, and the nonlinearity is captured in the simulation.

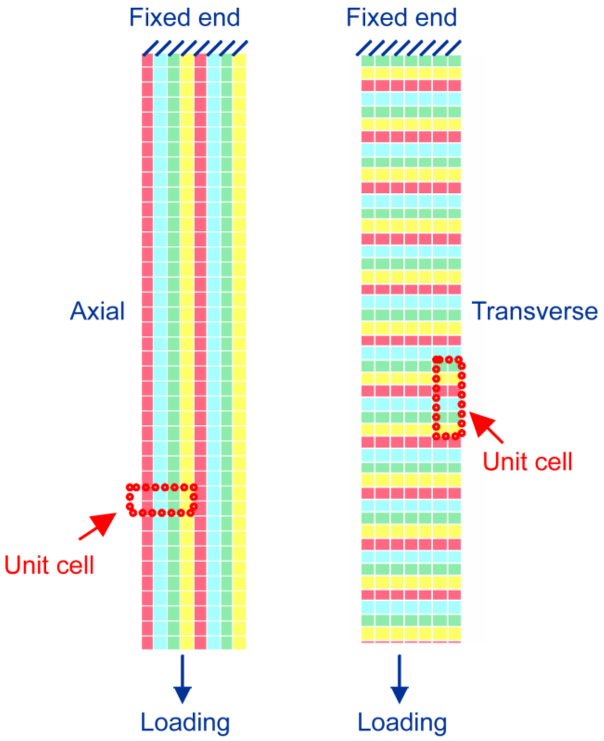

Figure 7.—Finite element models of axial tension (left) and transverse tension (right) tests (Ref. 2).

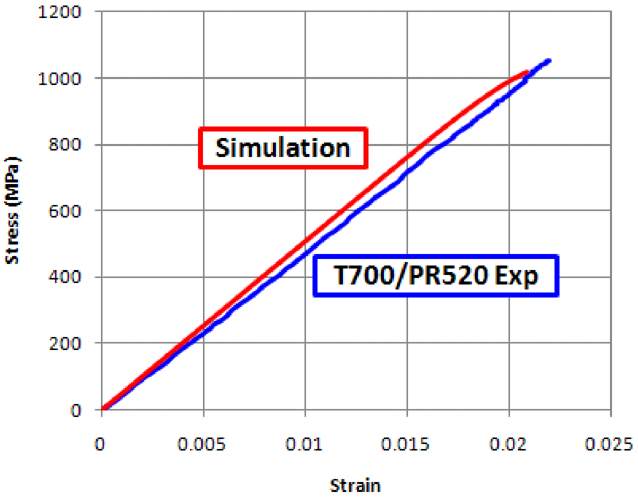

Figure 8.—Axial tension experimental versus computed response for T700/PR520 composite coupon test.

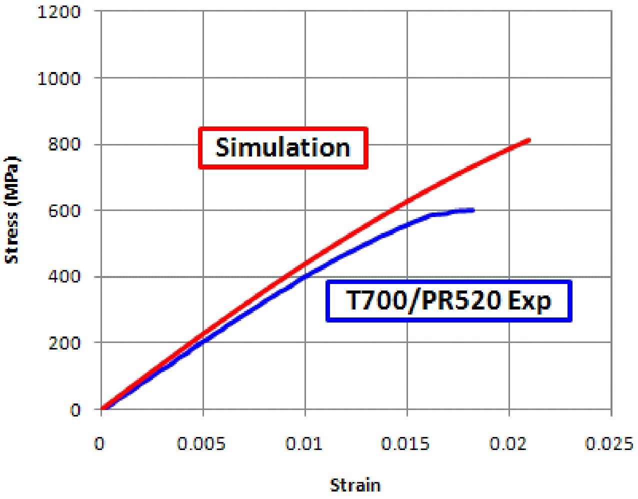

Figure 9.—Transverse tension experimental versus computed response for T700/PR520 composite coupon test.

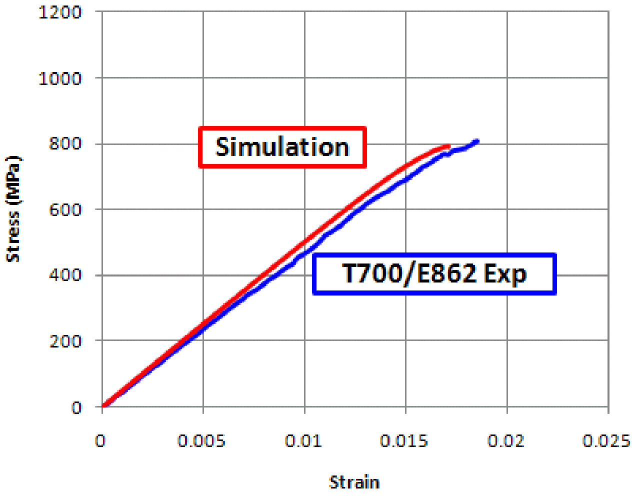

Figure 10.—Axial tension experimental versus computed response for T700/E862 composite coupon test.

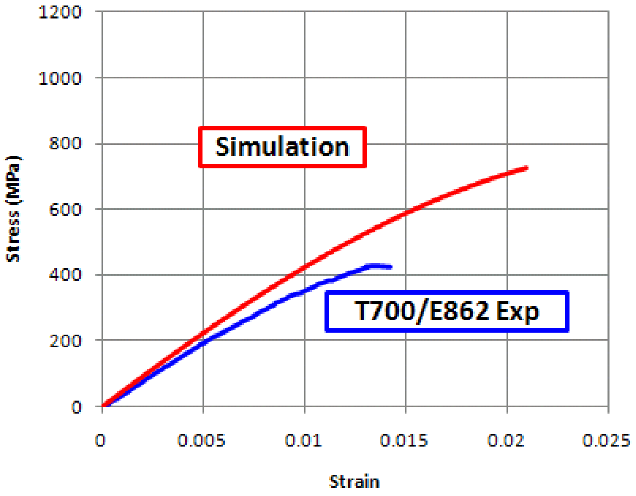

Figure 11.—Transverse tension experimental versus computed response for T700/E862 composite coupon test.

The transverse tension experimental results were not used in the material property calculations because composite transverse tensile tests conducted on straight-sided coupons may not yield results that are truly representative of the actual material strength response. As can be seen in the figures the initial stiffness of the axial and transverse experimental curves are the same, the transverse tension results become nonlinear at a much lower stress than the axial tension results. Theoretically, due to the quasi-isotropic material properties these curves should be much more similar. There has been some investigation in how the premature failure near the fiber bundles that terminate at free edges can contribute to the overall nonlinearity noted in the resulting curves. More discussion about the transverse tension coupon tests can be found in Reference 13. Because the goal is to capture in situ properties of large composite structures, these edge effects are not included in the simulations. Therefore, only the initial stiffness can be reasonably compared with the experimental test, while the experimental strength and stiffness are much lower than those of the simulations. Following the trends observed in the axial tensile results, the computed transverse tension T700/PR520 composite coupon simulation resulted in the highest strength of the transverse coupon simulations as shown in Figure 9. This result is expected because the properties (Table 3) for this material were the highest of the four. The computed transverse tension T700/E862 composite coupon simulation resulted in the second highest strength of the transverse coupon simulations after the T700/PR520 simulation as shown in Figure 11. This result correlates well quantitatively with the input properties. As shown in Figure 12, for the T700/5208 material the computed transverse tension composite coupon simulation results in the third highest strength of the four materials and, as shown in Figure 15, the computed transverse tension T700/3502 composite coupon simulation yields the lowest transverse tension strength of the four materials. Overall, for all four materials the ultimate transverse tension strengths obtained in the simulations are slightly lower than the axial tension strengths, which correlated well with the expected material behavior. The simulated curves also display a significant amount of nonlinearity, which also correlates well with the expected material response.

Axial and transverse compression simulations were carried out for the T700/PR520 and T700/E-862 materials using the same basic geometry and boundary conditions as shown in Figure 7 (only with compression loading as opposed to tensile loading). The simulated results were compared to experimental values obtained from quasi-static compression testing conducted by Littell (Ref. 13). The axial compression simulations compared well with experimental coupon testing results. These can be seen in Figure 16 and Figure 18. The transverse compression simulations also compared well with experimental coupon testing results. The comparison of the transverse compression simulations with the experimental results can be seen in Figure 17 and Figure 19. Both the stiffness and strength correlate well for both examined materials for the cases of both axial and transverse compression.

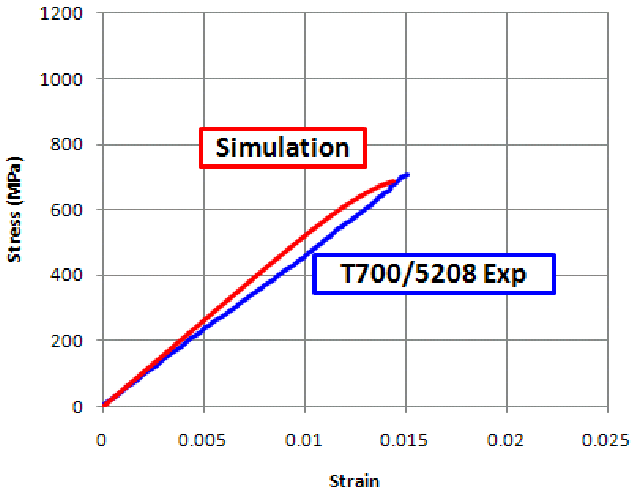

Figure 12.—Axial tension experimental versus computed response for T700/5208 composite coupon test.

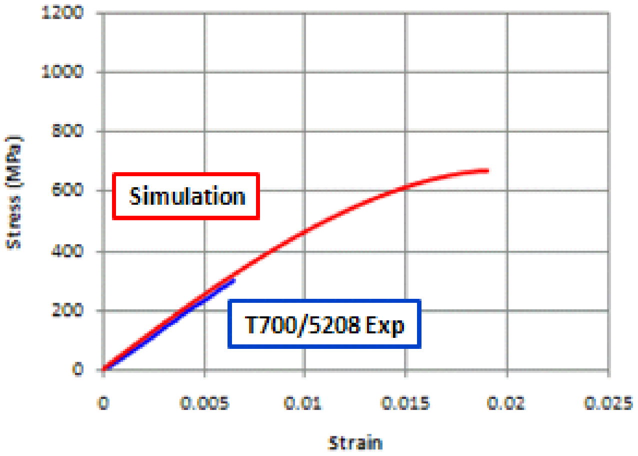

Figure 13.—Transverse tension experimental versus computed response for T700/5208 composite coupon test.

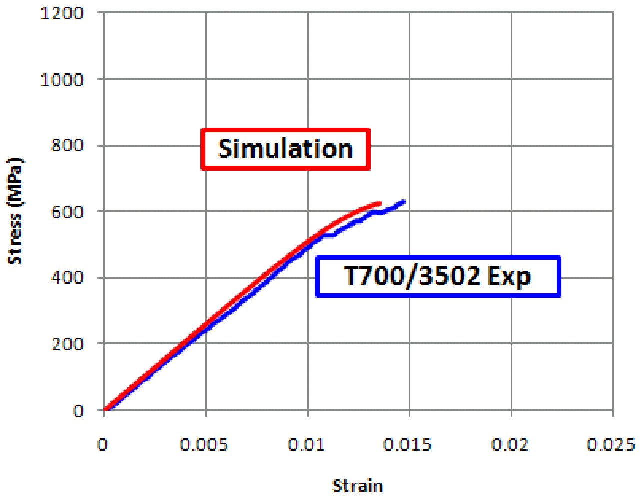

Figure 14.—Axial tension experimental versus computed response for T700/3502 composite coupon test.

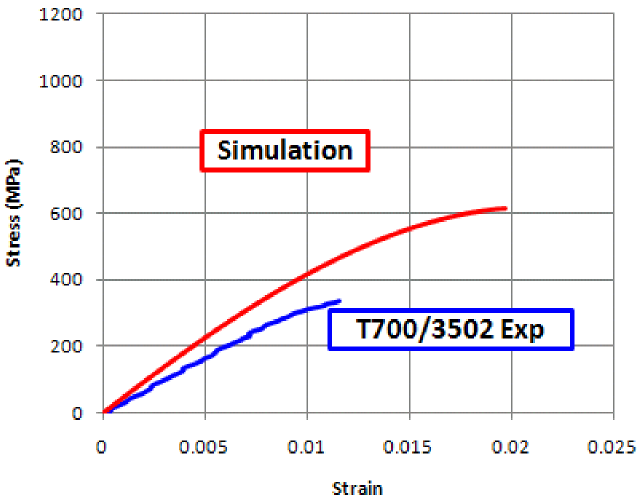

Figure 15.—Transverse tension experimental versus computed response for T700/3502 composite coupon test.

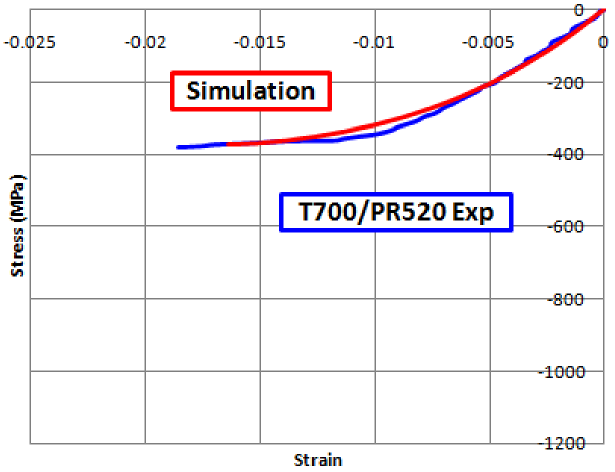

Figure 16.—Axial compression experimental versus computed response for T700/PR520 composite coupon test.

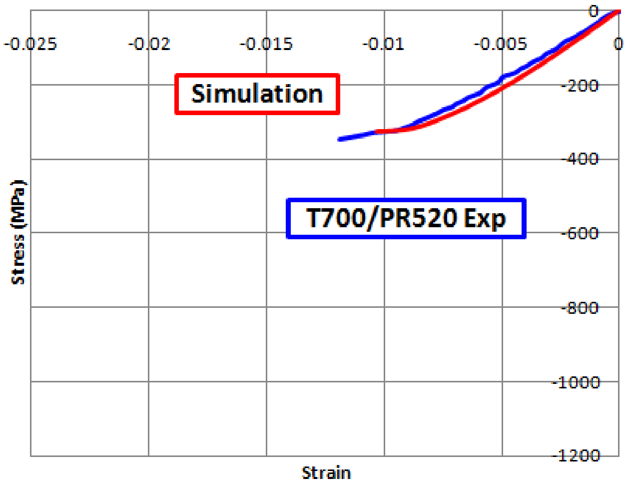

Figure 17.—Transverse compression experimental versus computed response for T700/PR520 composite coupon test.

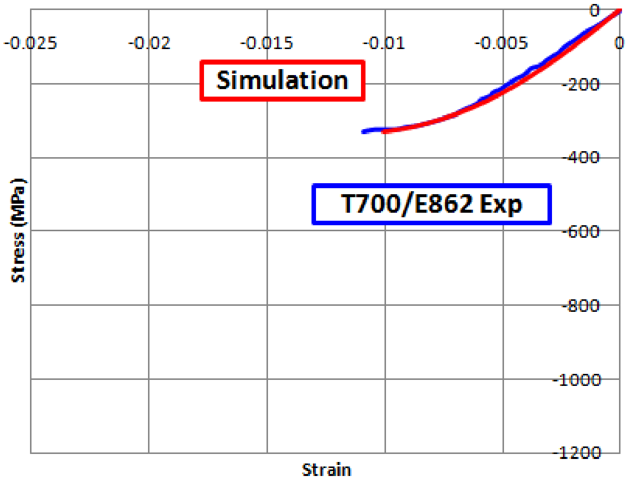

Figure 18.—Axial compression experimental versus computed response for T700/E862 composite coupon test.

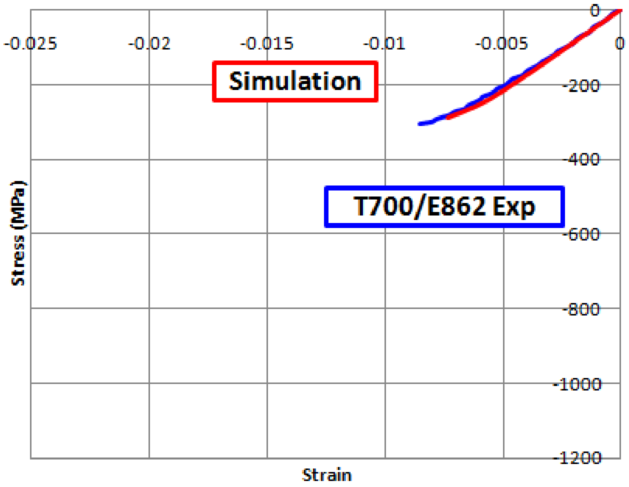

Figure 19.—Transverse compression experimental versus computed response for T700/E862 composite coupon test.

Integration Point Study

To examine the predictive capability of the analysis approach, impact tests conducted by Pereira, et al. (Ref. 21) were simulated. Since all of the characterization was conducted based on results from the quasi-static coupon tests, the impact simulations discussed in this section of the report are truly predictive. The impact tests, which were conducted in the NASA Glenn Research Center Ballistic Impact Laboratory, utilized a single-stage compressed gas gun to propel an aluminum 2024 projectile into 0.305- by 0.305- by 0.0032-m composite panels composed of six layers of the T700/E862 composite. The other materials have not been tested at the current time. The composite panel was held in a circular fixture with an aperture of 0.254 m. The projectile was a thin-walled hollow cylinder with a nominal mass of 50 gm and a front face with a compound radius. The overall length of the projectile was 0.0495 m, the wall thickness was 0.00076 m and the nominal diameter was 0.05067 cm. Tests were performed over a range of impact velocities to determine the velocity for the onset of damage, the growth of damage with increasing velocities, the penetration threshold, and the damage pattern induced by penetration. Twelve panel tests were conducted using impact velocities ranging from 157 to 175 m/s. The threshold velocity for penetration was determined to be between 161 and 168 m/s.

First, the number of integration points was analyzed for the quasi-static coupon simulations. These simulations were conducted with the number of through-thickness integration points ranging from 2 to 8. There was no difference between any of the quasi-static coupon simulations. This was determined to be due to the lack of out-of-plane deformation in the quasi-static coupon simulation (which reflects the test results). After this, the number of integration points was analyzed for the impact simulations (described in the next section of this report). For the impact simulations the number of through-thickness integration points was started at 2 and then increased until the solutions converged. There was no difference between the impact simulations using 12 and 13 integration points. Therefore, 12 integration points through-the-thickness were then used for all the simulations used in this analysis. All quasi-static and impact simulation results reported in this paper were run using 12 integration points which amounts to 2 integration points per braid layer.

Impact Predictions

After the material properties for each of the composites examined in this study were determined using the “Independently Homogenized Subcells” program and correlated using quasi-static coupon tests, simulation of impact tests conducted by Pereira, et al. (Ref. 22) were conducted. The high velocity impact tests were performed using a hollow hemispherical projectile (Ref. 22). Only one of the material systems examined in this paper, T700/E862, has undergone impact testing. The set-up for the impact simulation can be seen in Figure 20. The composite mesh simulated in the impact analysis had dimensions and constraints replicating those of the experiments. The panels were 30.5- by 30.5-cm (1- by 1-ft) squares with clamped boundaries in 25.4 cm (10 in.) diameter circles centered in the panels. The nodes in the circular boundary had all six degrees of freedom constrained. The panels were made up of 810 unit cells; 15 unit cells across and 54 unit cells vertically. Because there were four elements in a unit cell, the panel had 2700 elements, and 2805 nodes. The projectile was modeled as a linear elastic material to accurately account for energy absorption due to elastic deformation of the projectile. This was assumed due to the negligible amount of plastic deformation seen in the projectiles during testing. The density and stiffness of the projectile in the simulation were measured from the aluminum used in the experimental testing. The contact card employed was the LS-DYNA contact “*Contact_Automatic_ Single_Surface” (Ref. 12).

Figure 21 displays a comparison between the impact simulation and the experimental impact test. The black and white image is test specimen after impact. The black and white textured surface is painted on prior to testing to create a grid that is used in the digital image mapping process. There are two predictions to point out in Figure 21. The first notable item is the prediction of penetration velocity. The simulation predicted penetration of the projectile at 160 m/s (525 ft/s) which was slightly below the experimental threshold velocity range of 162 to 171 m/s (530-560 ft/s). The discrepancy in velocities is within 1 percent and therefore fairly reasonable.

The second item of note is the simulation's prediction of the damage pattern. There are a few limitations when comparing the simulations with experimental impact results. First, the experimental image displayed in Figure 21 is the image of panel post-testing. Because of this, it is difficult to assess the mode of initial failure and failure propagation in the experimental impact data. Second, there is a great deal of scatter in the data, as with most high velocity impact testing, and therefore the failure patterns differ greatly from test to test even though the ballistic limit has been identified within a reasonably tight range. In the experimental impact test specimen, the composite failure area appears to be shaped like an oval with more damage along the axial fibers (Figure 21). The simulation provides more detail on the initiation and propagation of damage. The initial area where failure propagates through all six layers of composite occurs in the lower left corner of the impact zone. From this point the failure begins to propagate, first along the bias fibers and then vertically along the axial fibers and finally horizontally. The projectile continues to damage the composite by folding back petals of the fractured region. The macro-scale simulation cannot capture fiber bundle splintering, but it can be interpreted as one of the physical mechanisms simulated by the petaling. The overall damage pattern in the experiment is slightly more elongated than the damage pattern seen in the simulation. However, it is safe to say that the simulation damage pattern is far closer to the experimental than a typical homogenized damage pattern where a perfect cross is formed. It is possible the difference could be due, again, to the use of quasi-static properties. There may be some anisotropic stiffening due to rate effects.

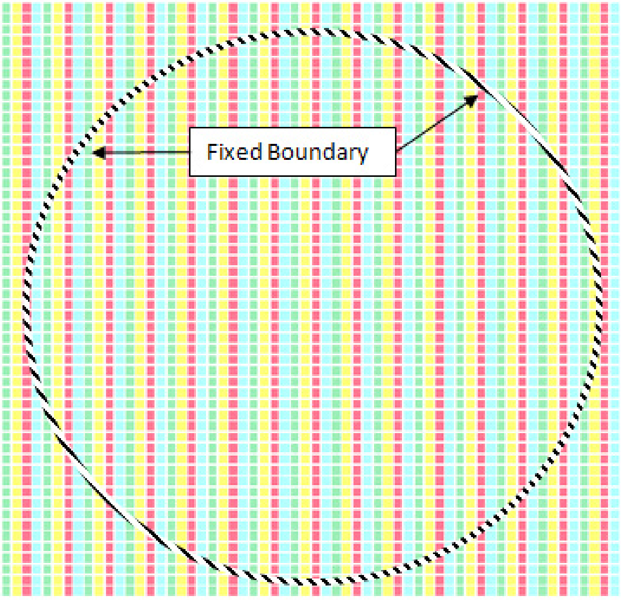

Figure 20.—Finite element mesh for impact simulations.

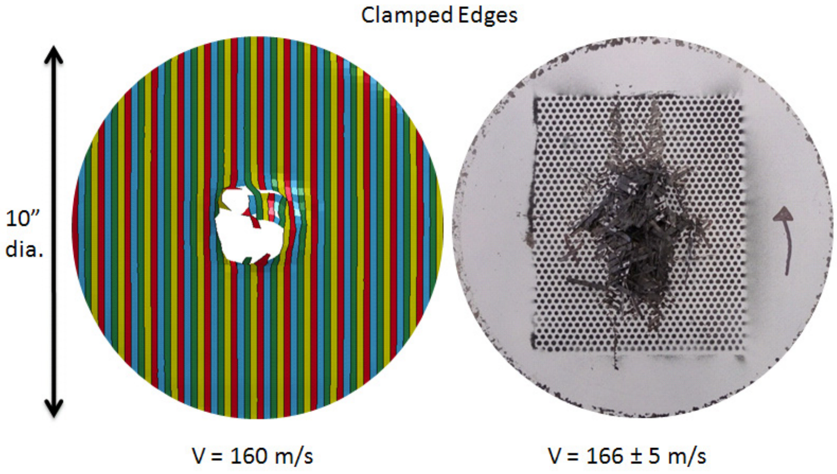

Figure 21.—Simulated (left) and experimental (right) damage patterns for T700/E-862 composite in impact (Ref. 20).

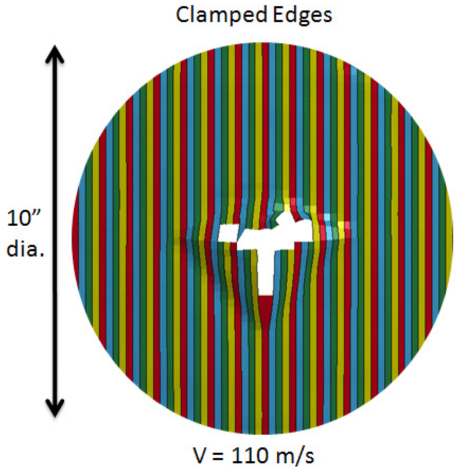

Figure 22.—Simulated damage patterns for T700/5208 composite in impact.

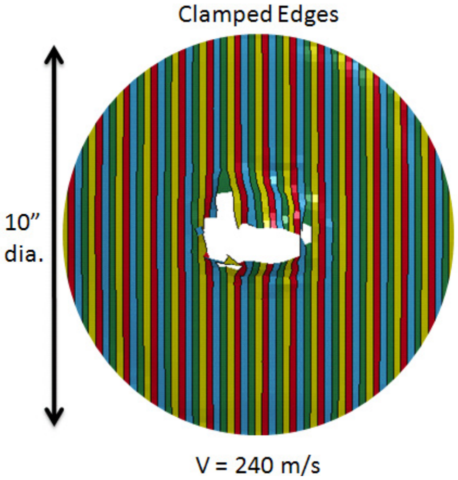

Figure 23.—Simulated damage patterns for T700/PR520 composite in impact.

High velocity impact simulations were conducted for the other three materials by using the same simulation setup. Here they are only examined qualitatively as there is no experimental data currently available to compare with directly. The T700/PR520 material had a ballistic limit of 240 m/s (775 ft/s) as seen in Figure 22. This was higher than the ballistic limit noted in the T700/E862 material simulation. The damage in the T700/PR520 simulation formed in a completely different way than the damage in the previous simulation. The damage initiated at the bottom center of the impact zone and propagated, first in both horizontal directions, and second upwards along the edges of the zone vertically cutting out a door-like flap of the composite plate. The initiation of vertical damage on the right side of the impact zone can be seen in the time step displayed in Figure 23. The T700/5208 material had a ballistic limit of 110 m/s (350 ft/s) as seen in Figure 23. This was the lowest ballistic limit of the examined materials and may be due to the low compression properties used in the "Independently Homogenized Subcells" program. In this simulation the failure initiated in the center of the impact zone and first propagated along the +60 bias fibers. The material continued to fail vertically and horizontally. The three petals that fold back during failure can be seen in Figure 23. The T700/3502 material had a ballistic limit of 150 m/s (500 ft/s) as seen in Figure 24. Damage propagation, again, occurred in a different way than the previous simulations. Damage in this simulation initiated in the center right of the impact zone and quickly propagated along the bias fibers both above and below the damaged area. While damage propagated in the horizontal direction, a new area of damage initiated in the center of the impact zone. This resulted in the damage of nearly all material in the impact zone. Because of this, no petaling occurred. This result differed from all the simulations with the other materials. The varying predicted damage patterns of the different materials show that material and architecturally-dependent damage mechanisms have been captured by the method. These simulations are also purely predictive because there has been no correlation on the impact level.

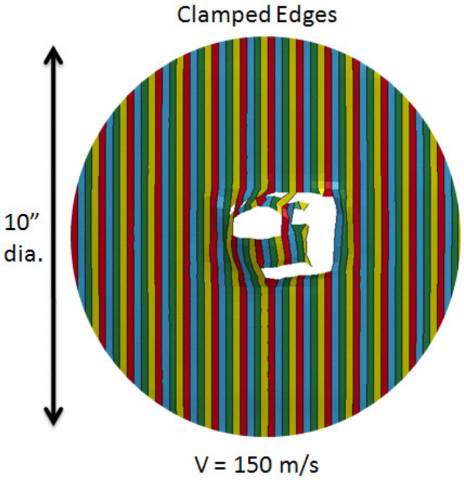

Figure 24.—Simulated damage patterns for T700/3502 composite in impact.

Conclusion

A macro level finite element-based approach has been developed that allows for the simulation of the response of a triaxially-braided composite in a manner that takes into account the architecture of the braided material within a structure. The input material properties utilized for the analysis can be determined based on experimental tests conducted on the braided composite. Quasi-static tension and compression tests on four representative composite materials were simulated, and the correlation between the analysis results and the experimental tests was reasonably good. Representative flat-panel impact tests were also simulated using the analysis model. Since the input material parameters were correlated based on the coupon level tests, these simulations were purely predictive. For the one material system where experimental data was available, the predicted ballistic limit was only slightly below the experimental value. The predicted impact damage patterns followed the details of the braided architecture, and were similar to the experimental damage patterns. The predicted impact damage patterns for the four material systems examined in this study were significantly different, indicating that the analysis method could capture the effects of differing material strengths on the impact damage in the material. Overall, the analysis method appears promising in its ability to simulate the architecturally-dependent impact damage in braided polymer matrix composites. Future efforts will involve incorporating the effects of strain rate into the model, modifying the method to allow for more general textile composite geometries, as well as investigating in more detail the capability of the model to simulate impact events, particularly before final penetration occurs.

References

1. Chou, T.W. and Ishikawa, T.: "Analysis and Modeling of Two-Dimensional Fabric Composites," in Textile Structural Composites, Composite Material Series, Vol. 3, T.W. Chou and F.K. Ko, Eds., Elsevier Science Publishers B.V., Amsterdam, 1989, Ch. 7, pp. 209-277.
2. Naik, N.K.; and Shembedkar, P.S.: "Elastic Behavior of Woven Fabric Composites: I-Lamina Analysis", Journal of Composite Materials, Vol. 26, No. 15, pp. 2196-2225, 1992.
3. Pastore, C.M. and Gowayed, Y.A.: "A Self-Consistent Fabric Geometry Model: Modifications and Application of a Fabric Geometry Model to Predict the Elastic properties of Textile Composites", Journal of Composites Technology and Research, Vol. 16, No.1, pp.32-36, 1994.
4. Byun, J.-H.: "The analytical characterization of 2-D braided textile composites", Composites Science and Technology, Vol. 60, No. 5, pp. 705-716. 2000.
5. Rao, M.P, Sankar, B.V., and Subhash, G.; Effect of Z-yarns on the stiffness and strength of three-dimensional woven composites, Composites: Part B, Vol. 40, pp. 540-551, 2009.
6. Walter, T.R., Subhansh, G., Sankar, B.V., and Yen, C.F.; Monotonic and cyclic short beam shear response of 3D woven composites. Composites Science and Technology, Vol. 70, No. 15, pp. 2190-2197, 2010.
7. Tanov, R. and Tabiei, A.: "Computationally Efficient Micromechanical Models for Woven Fabric Composite Elastic Moduli", Journal of Applied Mechanics, Vol. 68, No. 4, pp.553-560, 2001.
8. Bednarcyk, B.A.; and Arnold, S.M.: "Micromechanics-Based Modeling of Woven Polymer Matrix Composites", AIAA Journal, Vol. 41, No. 9, pp. 1788-1796, 2003.
9. Sankar, B.V.; and Marrey, R.V.: "Analytical Method for Micromechanics of Textile Composites", Composites Science and Technology, Vol. 57, pp.703-713, 1997.
10. Jenq, S.T.; and Mo, J.J.: "Ballistic Impact Response for Two-Step Braided Three-Dimensional Textile Composites", AIAA Journal, Vol. 34, No. 2, pp. 375-384, 1996.
11. Cheng, J., "Material Modeling of Strain Rate Dependent Polymer and 2D Triaxially Braided Composites", Ph.D. Dissertation. University of Akron. Akron, Ohio. 2006.
12. Hallquist, J.O. et al., "LS-DYNA Keyword User's Manual", Livermore Software Technology Corporation, Livermore, CA, May 2007.
13. Littell, J., "The Experimental and Analytical Characterization of the Micromechanical Response for Triaxial Braided Composite Materials", Ph.D. Dissertation. University of Akron. Akron, Ohio. 2008.
14. Littell, J.D.; Binienda, W.K.; Roberts, G.D.; and Goldberg, R.K.: "Characterization of Damage in Triaxial Braided Composites under Tensile Loading", Journal of Aerospace Engineering, Vol. 22, No. 3, pp. 270-279, 2009.
15. Li, X.; Binienda, W.K.; and Goldberg, R.K.: "Finite Element Model for Failure Study of Two-Dimensional Triaxially Braided Composite." NASA/TM-2010-216372, 2010.
16. Xiao, X.; Kia, H.G.; and Gong, X.-J.: "Strength prediction of a triaxially braided composite", Composites: Part A, Vol. 42, pp. 1000-1006, 2011.
17. Matzenmiller, A., Lubliner, J., Taylor, R.L. "A constitutive model for anisotropic damage in fiber-composites", University of California at Berkeley. Berkeley, CA. 1994.
18. Hashin, Z., "Failure Criteria for Unidirectional Fiber Composites", *J. Appl. Mech*. 47, 329. 1980.
19. Liu, K.C.; Chattopadhyay, A.; Bednarcyk, B.A.; and Arnold, S.M.: "Efficient Multiscale Modeling Framework for Triaxially Braided Composites Using Generalized Method of Cells", Journal of Aerospace Engineering, Vol. 24, No. 2, pp. 162-169, 2011.
20. Goldberg, R.K., Roberts, G.D. and Gilat, A.; Implementation of an Associative Flow Rule Including Hydrostatic Stress Effects into the High Strain Rate Deformation Analysis of Polymer Matrix Composites, J. Aerospace Eng., Vol. 18, pp. 18-27, 2005.
21. Jones, R.M., *Mechanics of Composite Materials,* 2nd ed., Taylor & Francis, Philadelphia, 1999, Chap. 4.
22. Pereira, J.M.; Roberts, G.D.; Ruggeri, C.R.; Gilat, A.; and Matrka, T., "Experimental Techniques for Evaluating the Effects of Aging on Impact and High Strain Rate Properties of Triaxial Braided Composite Materials", NASA/TM—2010-216763, 2010.

REPORT DOCUMENTATION PAGE	*Form Approved* *OMB No. 0704-0188*

1. REPORT DATE *(DD-MM-YYYY)* 01-07-2012	**2. REPORT TYPE** Technical Memorandum	**3. DATES COVERED** *(From - To)*

4. TITLE AND SUBTITLE Macro Scale Independently Homogenized Subcells for Modeling Braided Composites	**5a. CONTRACT NUMBER**
	5b. GRANT NUMBER
	5c. PROGRAM ELEMENT NUMBER
6. AUTHOR(S) Blinzler, Brina, J.; Goldberg, Robert, K.; Binienda, Wieslaw, K.	**5d. PROJECT NUMBER**
	5e. TASK NUMBER
	5f. WORK UNIT NUMBER WBS 284848.02.02.03.01.02
7. PERFORMING ORGANIZATION NAME(S) AND ADDRESS(ES) National Aeronautics and Space Administration John H. Glenn Research Center at Lewis Field Cleveland, Ohio 44135-3191	**8. PERFORMING ORGANIZATION REPORT NUMBER** E-18209
9. SPONSORING/MONITORING AGENCY NAME(S) AND ADDRESS(ES) National Aeronautics and Space Administration Washington, DC 20546-0001	**10. SPONSORING/MONITOR'S ACRONYM(S)** NASA
	11. SPONSORING/MONITORING REPORT NUMBER NASA/TM-2012-217621

12. DISTRIBUTION/AVAILABILITY STATEMENT
Unclassified-Unlimited
Subject Categories: 24 and 39
Available electronically at http://www.sti.nasa.gov
This publication is available from the NASA Center for AeroSpace Information, 443-757-5802

13. SUPPLEMENTARY NOTES
Submitted to the AIAA Journal.

14. ABSTRACT

An analytical method has been developed to analyze the impact response of triaxially braided carbon fiber composites, including the penetration velocity and impact damage patterns. In the analytical model, the triaxial braid architecture is simulated by using four parallel shell elements, each of which is modeled as a laminated composite. Currently, each shell element is considered to be a smeared homogeneous material. The commercial transient dynamic finite element code LS-DYNA is used to conduct the simulations, and a continuum damage mechanics model internal to LS-DYNA is used as the material constitutive model. To determine the stiffness and strength properties required for the constitutive model, a top-down approach for determining the strength properties is merged with a bottom-up approach for determining the stiffness properties. The top-down portion uses global strengths obtained from macro-scale coupon level testing to characterize the material strengths for each subcell. The bottom-up portion uses micro-scale fiber and matrix stiffness properties to characterize the material stiffness for each subcell. Simulations of quasi-static coupon level tests for several representative composites are conducted along with impact simulations.

15. SUBJECT TERMS
Polymer matrix composites; Braided composites; Finite element method; Micromechanics

16. SECURITY CLASSIFICATION OF:			**17. LIMITATION OF ABSTRACT**	**18. NUMBER OF PAGES**	**19a. NAME OF RESPONSIBLE PERSON** STI Help Desk (email:help@sti.nasa.gov)
a. REPORT U	**b. ABSTRACT** U	**c. THIS PAGE** U	UU	24	**19b. TELEPHONE NUMBER** *(include area code)* 443-757-5802